Spectroscopic Ellipsometry Investigation of CuInSe₂ as a Narrow Bandgap Component of Thin Film Tandem Solar Cells

Dhurba R. Sapkota, Prakash Koirala, Puja Pradhan, Niraj Shrestha, Maxwell M. Junda, Adam B. Phillips, Randy J. Ellingson, Michael J. Heben, Sylvain Marsillac*, Nikolas J. Podraza, and Robert W. Collins

Wright Center for Photovoltaics Innovation & Commercialization, Univ. Toledo, Toledo, Ohio, 43606, USA; * Virginia Institute of Photovoltaics, Old Dominion Univ., Norfolk, Virginia, 23529, USA

Abstract — Spectroscopic ellipsometry (SE) was performed on CuInSe₂ (CIS) thin films and solar cells with a goal toward optimizing this low bandgap absorber for tandem applications. The CIS thin films and the absorbers in devices were deposited by one-stage thermal co-evaporation on silicon and on Mo-coated soda-lime glass substrates in a deposition system that has yielded $CuIn_{1-x}Ga_xSe_2$ (CIGS) cells with > 17% efficiency using standard thickness (2.0 μ m) x = 0.3 absorbers and > 13% using 0.7 μ m low-Ga absorbers. In this study, a mapping capability for CIS Cu stoichiometry y = [Cu]/[In] over the film area was established based on a y-dependent parametric dielectric function (ε_1 , ε_2) with bandgap critical point E_g decreasing linearly from 1.030 eV for y = 0.7 to 1.016 eV for y = 1.1. In addition, a full set of $(\varepsilon_1, \varepsilon_2)$ spectra measured for the CIS cell components enables analysis of SE data in terms of an accurate structural model for the device. With this model, spectra in the external quantum efficiency can be predicted, and deviations from this prediction can be attributed to incomplete collection of photogenerated electrons and holes as simulated with a carrier collection profile.

Index terms — ellipsometry, photovoltaic cells, semiconductor films, semiconductor device modeling

I. INTRODUCTION

CuInSe₂ (CIS) and related materials have been studied intensively for applications as the absorber layers of solar cells [1-8]. These materials have favorable electronic and optical properties including a direct bandgap, strong absorption, and controllable p-type conductivity. The first such solar cells were fabricated by evaporation of n-type CdS onto p-type CIS bulk crystals, reported by Shay $et\ al$. in 1974 [6]. For the first fully thin-film CuInSe₂/CdS devices, absorbers were deposited by CIS and Se co-evaporation and led to a ~ 6 –7% efficiency, reported by Kazmerski $et\ al$. in 1976 [7]. Attention was drawn to cells from CIS and related materials upon demonstration of a 9.4% device by Mickelsen $et\ al$. in 1981 [8].

Because of its controllable p-type conductivity by varying copper stoichiometry, its adjustable bandgap by alloying with gallium, and its high stability, the CIS-based system is one of the two most widely commercialized absorber technologies for thin film solar cells. Currently, devices fabricated using thin film CIGS as an absorber layer with [Ga]/{[In]+[Ga]} ~ 0.3 and a bandgap near 1.2 eV exhibit a laboratory-scale record efficiency of 22.6% [9]. Most high efficiency CIS-based solar cells have been prepared using window layers of CdS, which leads to a reduction in the achievable current due to absorption at photon energies above the CdS bandgap.

Because CIS is among the narrowest bandgap thin film absorber materials (~1.0 eV) that have led to efficient solar cells, this absorber is a suitable candidate for the bottom cell of tandem devices. In fact, the CdS window layers widely used for efficient CIS devices do not have a negative impact on bottom cell performance because photons of energy above the window layer bandgap are absorbed by the top cell. More recently, significant progress has been made in the performance of devices with either CIS or CIGS as the bottom cell in tandem structures [10]. Performance modeling of monolithic CIS/perovskite tandems indicates that efficiencies > 30% are possible [11]. An efficiency of 10.9% has been reported for such a CIGS/perovskite tandem device [12].

For large area CIS or CIGS modules, the absorber layer properties are likely to depend on the spatial position within the plane of the module. These variations are expected due to process non-uniformity over large areas. Although detrimental in manufacturing, non-uniformity in the research laboratory provides opportunities for cell optimization in terms of basic properties. Using spectroscopic ellipsometry (SE) mapping and correlating the resulting material properties with the cell performance, location by location, a clearer understanding of the specific properties that optimize solar cells can be obtained [13]. SE-deduced maps describing the complete solar cell structure also enable calculation of maps in the local current density generated by the device assuming all electrons and holes generated within the active device layers are collected.

II. EXPERIMENTAL DETAILS

The complex dielectric function spectra, $\varepsilon = \varepsilon_1 + i\varepsilon_2$, of CIGS depend on the alloy composition $x = [Ga]/\{[In] + [Ga]\}$ and stoichiometry $y = [Cu]/\{[In] + [Ga]\}$ and can be used as a metric for compositional analysis. Previously, a parametric analysis of ε versus gallium content x in CIGS with fixed copper content $y = 0.90 \pm 0.03$ has been reported that enables compositional profile mapping [13]. In the present article, mapping y for CIS (x = 0) will be reported with the potential for large area analysis. In the studies by SE mapping, a single CIS thin film with an intended thickness of ~ 60 nm was deposited on a 10 cm x 10 cm c-Si substrate using one-stage thermal co-evaporation in a high vacuum chamber with a base pressure of 2 x 10^{-6} Torr. The vapor flux rates of the individual elements were held constant using fixed source

°C, and the substrate was placed to ensure a wide variation in y of 0.6 < y < 1.2 over the film area due to the different source locations within the chamber. In studies by SE at a single location for structural and external quantum efficiency (EQE) analysis, the solar cells were obtained by depositing one-stage CIS to a thickness of $\sim 1.25~\mu m$ on Mo-coated soda-lime glass (SLG). The Mo was sputter-deposited on the SLG at $T_s = 250$ °C [14]. The solar cell was completed with layers of CdS deposited by chemical bath deposition (CBD), intrinsic ZnO

and Sn-doped In₂O₃ (ITO) both prepared by sputtering, and

silver top grids prepared by evaporation, the vapor depositions

being done at room temperature. The lower absorber thickness

relative to a 2 µm standard led to lower efficiencies, up to 7%.

temperatures. The substrate temperature was set at $T_s = 570$

The sample on the c-Si was characterized over its 10 cm x 10 cm area at 625 locations using a mapping SE system which employs a rotating-compensator multichannel ellipsometer (J. A. Woollam Co., M-2000 DI). The sample was then cut into pieces for analysis by electron microscopy with the capabilities of energy dispersive X-ray spectroscopy (EDS; Hitachi S-4800). Eight sample pieces for measurement were selected from locations that ensure a wide range of y. A representative complete solar cell was also measured by SE at 70° angle of incidence. The deduced structural model enabled EQE simulation for comparison with the measurement.

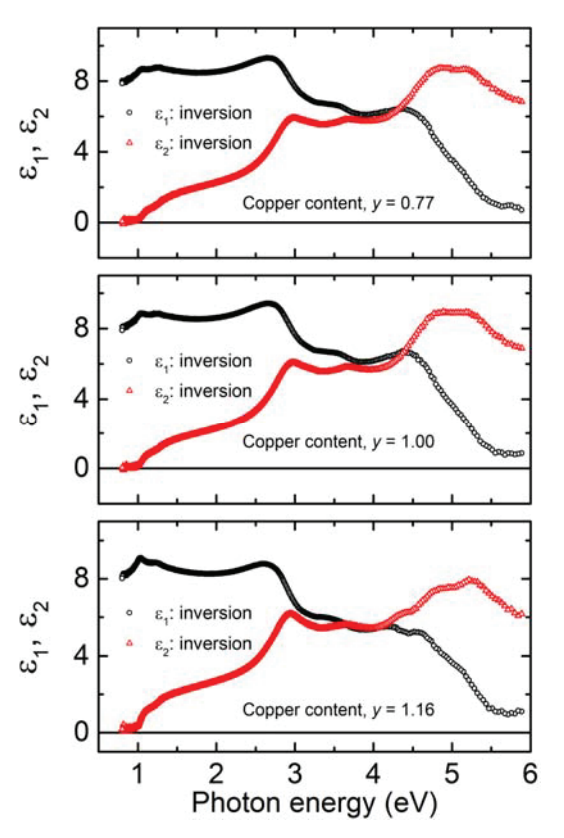


Fig. 1. Dielectric functions for thin film CIS with three different values of the copper content $y=0.77,\ 1.00,\$ and 1.16. In the determination of these results, best fit structural parameters were fixed and exact inversion of the SE data was performed.

III. RESULTS AND DISCUSSION

A. Mapping SE of CIS Material

Mapping SE data were analyzed assuming an optical model as follows: c-Si/(SiO₂ native oxide)/CIS/(surface roughness). A starting point complex dielectric function $(\varepsilon_1, \varepsilon_2)$ for the CIS layer was adopted from the results for a sample with x = $0, y = 0.90 \pm 0.03$ from Ref. [13]. Iterative adjustments were then made using a Kramers-Kronig consistent B-spline model. The $(\varepsilon_1, \varepsilon_2)$ spectra for the components of the c-Si substrate and the thickness of its native oxide were used from an existing database and from an SE measurement before deposition, respectively. The CIS bulk and surface roughness layer thicknesses and the void volume fraction in the roughness layer were the key outputs of the B-spline fit. The results for the best fit structural parameters were fixed in a final numerical inversion of SE data to generate the $(\varepsilon_1, \varepsilon_2)$ spectra for the CIS thin films. Figure 1 shows the resulting spectra for three locations with y values 0.77, 1.00, and 1.16. Figure 2 shows the second derivatives of the $(\varepsilon_1, \varepsilon_2)$ spectra of Fig. 1. The results in Fig. 2 were fit to an expression for $(\varepsilon_1,$ ε_2) assuming a sum of two critical point (CP) oscillators. The lower energy CP, $E_0(A,B)$, defines the bandgap E_g , and its best fit energy shows a monotonically decreasing trend with increasing Cu content y. Values in Fig. 2 are 1.026 eV for

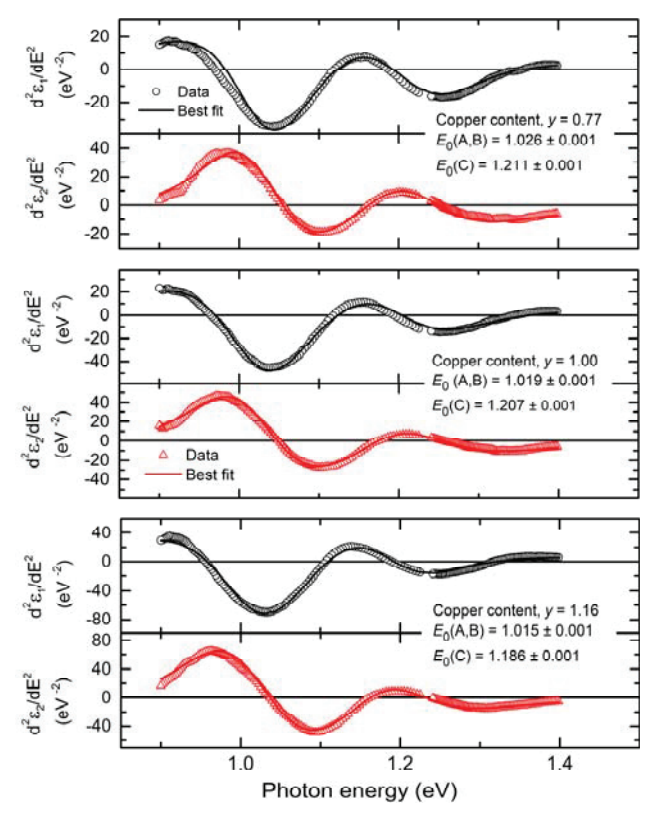


Fig. 2. Second derivatives of the complex dielectric functions of Fig. 1 for CIS thin films (points) along with best fits (lines) assuming a sum of two CP oscillators. The precise values of the energies for the bandgap CP $[E_0(A,B)]$ and near bandgap CP $[E_0(C)]$ are shown.

y = 0.77, 1.019 eV for y = 1.00, and 1.015 eV for y = 1.16. The next higher energy critical point $E_0(C)$ shows a similar decreasing trend with increasing y. The corresponding $E_0(C)$

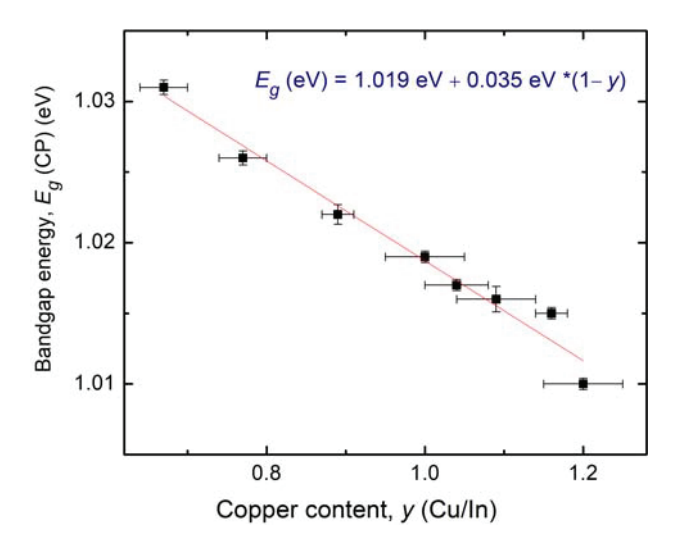


Fig. 3. Bandgap CP energy $E_g = E_0(A,B)$ for CIS thin films as a function of the copper content y obtained from analyses of second derivatives of the $(\varepsilon_1, \varepsilon_2)$ spectra such as those of Fig. 2.

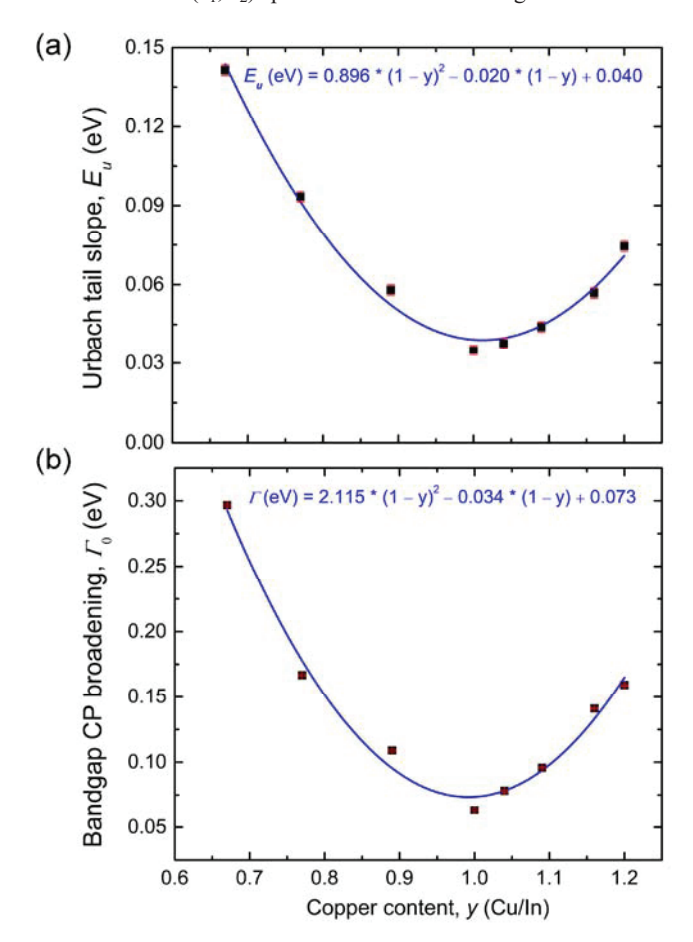


Fig. 4. Plots of (a) Urbach tail slope and (b) bandgap critical point broadening parameter versus copper content y obtained from $(\varepsilon_1, \varepsilon_2)$ spectra for the set of eight CIS films of Fig. 3.

values are 1.211 eV for y = 0.77, 1.207 eV for y = 1.00, and 1.186 eV for y = 1.16. All confidence limits are $\sim \pm 0.001$ eV. Figure 3 shows a plot of the resulting $E_0(A,B)$ CP bandgap E_g versus Cu content y from EDS for the full set of eight samples. The figure shows a decrease in bandgap with increasing y that is closely linear over the range of y from ~ 0.7 to 1.1.

The inverted dielectric functions were parameterized by using a combination of critical point (CP) oscillators and a broad background Tauc-Lorentz oscillator, along with a constant offset to ε_1 . Furthermore, an Urbach absorption tail was added so as to fit ε_2 below the bandgap. Figure 4 (a) and (b) show the resulting Urbach tail slope and bandgap CP broadening versus y, respectively. A close correlation between the two parameters is observed. Minima are found near y=1 in both plots, indicating that stoichiometric CIS exhibits the lowest disorder or potential fluctuations.

Figure 5 depicts optical gap energies for CIS obtained from the zero-ordinate extrapolation of the absorption edge region where $(\alpha nE)^2 \propto E$; in this proportionality α , n, and E are the absorption coefficient, the index of refraction, and the photon energy, respectively. These data are plotted versus the CP bandgap values from the second derivatives of the (ϵ_1, ϵ_2) spectra as in Fig. 2. The plot shows three regimes: (i) a linear segment for $y \ge 1.04$ where the extrapolation optical gap is lower than the CP bandgap, likely due to subgap absorption that occurs with excess Cu content and distorts the analysis by extrapolation; (ii) a linear segment with $0.77 \le y \le 1.04$ with excellent agreement between the two gap determinations; and (iii) a single result for y = 0.67 leading a higher extrapolation optical bandgap than the CP bandgap, generated by a change in the absorption onset shape observed for low y.

Figure 6 shows maps of the CIS layer effective thickness and the CIS composition and bandgap as obtained from SE analyses over the 10 cm x 10 cm sample area. The parametric form for $(\varepsilon_1, \varepsilon_2)$ given in terms of y enables simultaneous determination of the variations in the structural parameters and stoichiometry over the mapped area. The effective thickness in the top-most map of Fig. 6 is defined as the volume of CIS material per unit substrate area, given by $d_{\text{eff}} = d_b + (1 - f_v) d_s$, where d_b and d_s are the bulk and surface roughness layer thicknesses and f_{ν} is the void volume fraction in the surface roughness layer. The Cu content y in the center map of Fig. 6, determined from the parameterization, provides the bandgap energy in the lower map through the relationship of Fig. 3. The observed non-uniformity over the area of the sample, as measured by mapping SE, is intentional due to the positioning of the substrate and sources. In addition, the fluxes were set for excess Cu with $y \sim 1.2$ over the most uniform area of the substrate in order to achieve the desired wide range of y over the full area. The SE analysis results using the parametric (ε_1 , ε_2) were found to be closely consistent with EDS over the range $0.7 \le y \le 1.1$, as shown by the correlation plot in Fig. 7. Deviations occur for y > 1.1 where the parametric expressions for $(\varepsilon_1, \varepsilon_2)$ in terms of y are less accurate.

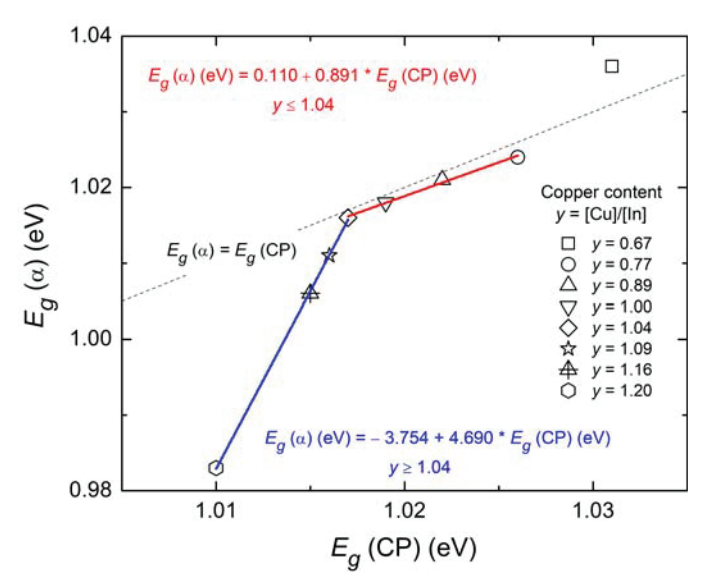


Fig. 5. CIS optical gaps from the $(\alpha n E)^2$ vs. E extrapolation versus bandgaps E_g obtained from the CP model. Here α is the absorption coefficient, n is the refractive index, and E is the photon energy.

B. Solar Cell and EQE Analysis

Figure 8 (points) shows the SE measurement results in the form of (ψ, Δ) for a complete CIS solar cell with the structure SLG/Mo/CIS/CdS/ZnO/ITO, where SLG indicates the sodalime glass substrate. In addition to the $(\varepsilon_1, \varepsilon_2)$ database for CIS developed as described in the previous section, an earlier database presented in detail elsewhere was used for the $(\varepsilon_1, \varepsilon_2)$ spectra of Mo, CdS, and ZnO [15]. The results for ITO were obtained from an individual film deposited on SLG using the procedures outlined in detail in Ref. [15]. The best fit to the SE spectra are shown in Fig. 8 as the solid lines with the deduced structural parameters given in the schematic of Fig. 9. This fit closely describes the data with the low energy interference fringes providing information on the CIS layer thickness and the high energy fringes providing information on the overlying layer thicknesses. Roughness layers are required on the surface of the ITO and at the Mo/CIS and CIS/CdS interfaces in order to obtain a high quality fit. These roughness layers are in general thicker than those on standard CIGS solar cells, likely due to thicker roughness on the 1.25 μm CIS layer compared to 2 μm CIGS. Because of the similarity of the $(\varepsilon_1, \varepsilon_2)$ spectra of ZnO and ITO, roughness at the interface between these two layers cannot be detected.

Figure 10 shows EQE spectra predicted from the structural model in Fig. 9 for comparison with the measurement. Two predictions are presented, one in which 100% collection of photogenerated electrons and holes in the two active layers are assumed, and the other in which reduced collection in the form of a step-wise profile is assumed for the CIS bulk layer. In the former simulation, the active layers are the CIS bulk layer and the CIS/CdS interface layer as in earlier studies [15].

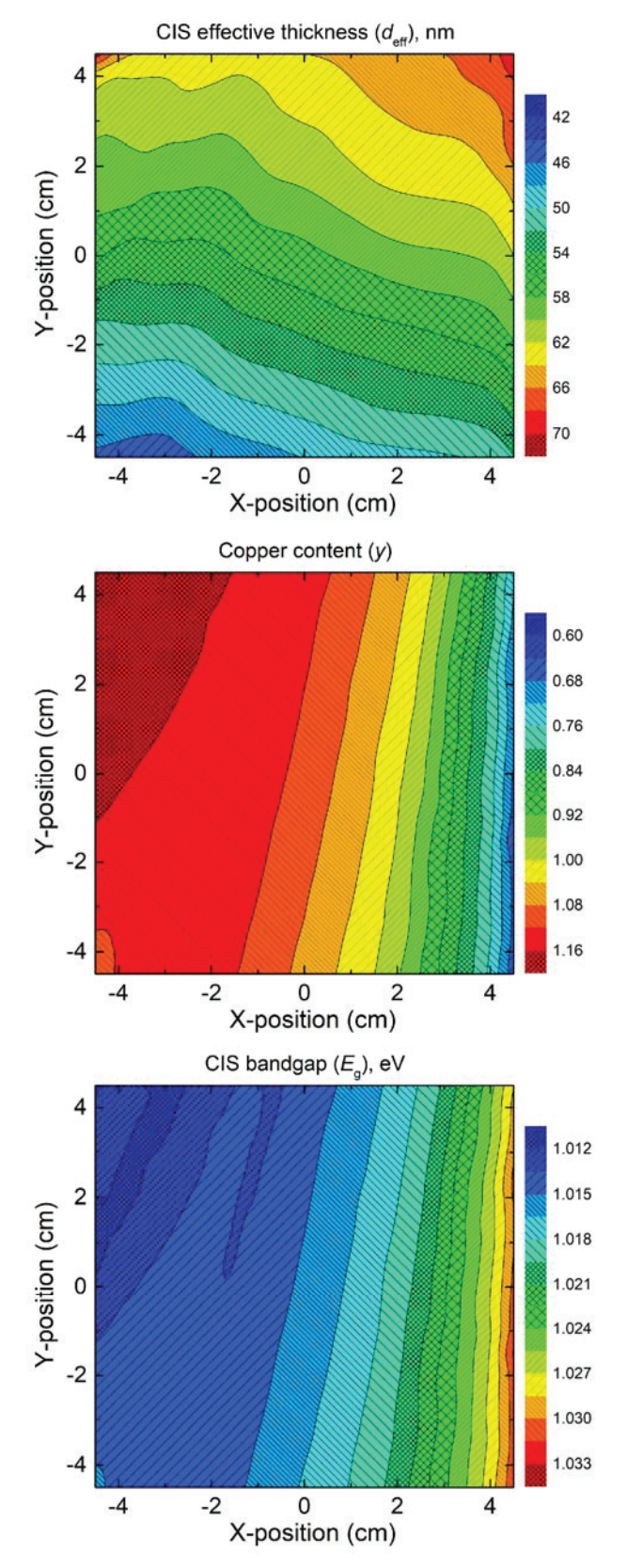


Fig. 6. Maps of (top) CIS effective thickness $d_{\rm eff}$, (center) Cu content y, and (bottom) bandgap energy E_g obtained simultaneously in an SE analysis of a thin CIS film deposited on a 10 cm x 10 cm c-Si wafer.

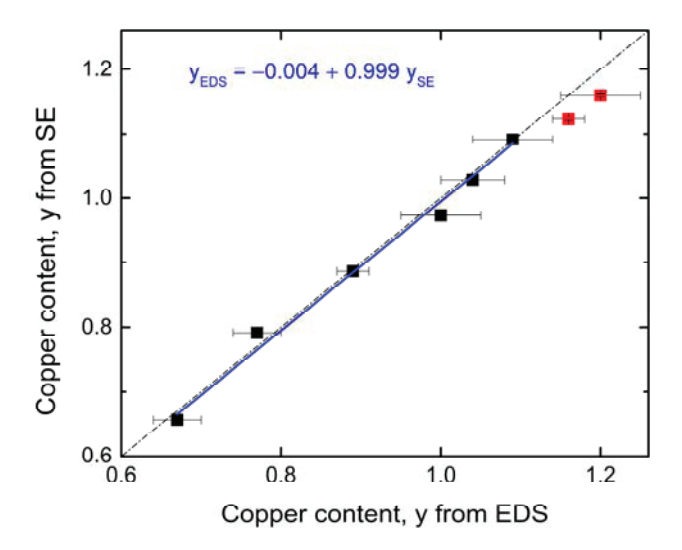


Fig. 7. Correlation between the Cu contents y deduced by SE and by EDS at the same location on the CIS sample. The SE results were obtained in a best fit to data from the map of Fig. 6 using a parametric expression for the (ϵ_1, ϵ_2) spectra with y as the single free parameter along with structural parameters of bulk and surface roughness layer thicknesses and surface roughness void content. The mapped thin film structure was deposited with an intended thickness of ~ 60 nm over a 10 cm x 10 cm c-Si substrate by using one-stage thermal co-evaporation.

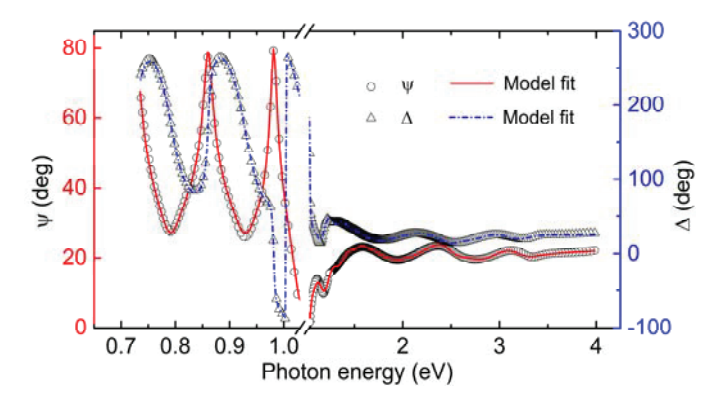


Fig. 8. SE data in the ellipsometry angles ψ (circles) and Δ (triangles) acquired at an angle of incidence of 70° for a completed CIS solar cell having the structure SLG/CIS/CdS/ZnO/ITO. A best fit (lines) is shown that provides the structural parameters in Fig. 9

A significant reduction in the measured EQE relative to the ideal simulation is observed. This difference can be reduced by assuming a carrier collection profile that varies from 100% collection close to the junction, dropping to zero in a layer \sim 250 nm thick adjacent to the back contact, behavior similar to that observed for cells with thin CIGS absorbers $< 1~\mu m$ [15]. The transition to < 50% collection occurs at ~ 500 nm distance from the junction, consistent with a reduced diffusion length for minority carriers in the CIS layer as compared to CIGS. Future efforts will focus on multistage and post-deposition processing to improve the CIS absorber layer properties.

Layer (composition, properties)	Thickness
surface roughness (f _v = 30.7%)	47.43 ± 1.07 nm
ITO (f _v = 0.0%)	67.43 ± 1.63 nm
i-ZnO/ITO ($f_{ZnO} = 50\%$, $f_v = 0.0\%$)	0.00 ± 3.02 nm
i-ZnO (f _v = 0.0%)	159.53 ± 2.00 nm
CdS/i-ZnO ($f_{CdS} = 48.4\%$, $f_v = 0.0\%$)	42.07 ± 1.63 nm
CdS (f _v = 0.0%)	32.23 ± 2.67 nm
CIS/CdS (f _{CIS} = 71.1%, f _v = 0.0%)	66.88 ± 0.95 nm
CIS (f _v = 0.0%)	1216.00 ± 1.27 nm
Mo/CIGS (f _{Mo} = 77.2%)	30.00 nm
Mo (opaque)	

Fig. 9. Solar cell schematic presenting the best fit structural parameters along with the confidence limits on the thicknesses, obtained in an analysis of the SE data shown in Fig. 8. This structure forms the basis of the EQE simulations in Fig. 10.

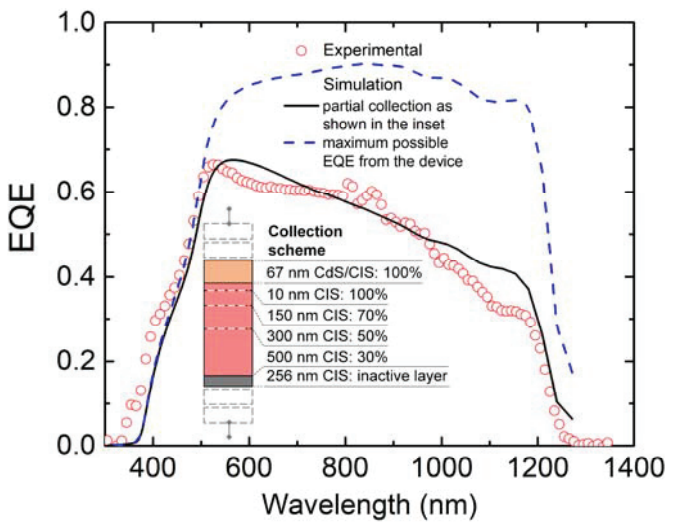


Fig. 10. Two EQE simulations along with experimental results for a CIS solar cell. The simulations were obtained using the structural model for the solar cell shown in Fig. 9. In one case (broken line) 100% collection of photogenerated electrons and holes is assumed from the two active layers, the CIS bulk layer and the CIS/CdS interface layer, and in the other case (solid line), a step-wise approximation to a collection profile shown in the inset is assumed.

IV. CONCLUSIONS

Ex-situ single-location and mapping SE have been implemented to characterize CIS thin films and devices. By exploiting a spatial variation in stoichiometry, a parametric expression for the complex dielectric function of CIS in terms of the copper content y = [Cu]/[In] has been established. This parametric expression enables large area mapping of thin films in terms of the bulk and surface roughness layer thicknesses, the effective thickness, and the Cu stoichiometry, the latter

showing spatial variations typically due to the positioning of metallic sources. From analyses of SE measurements performed on complete solar cells, structural models can be determined that enable simulations of the external quantum efficiency (EQE). Comparisons of these simulations with EQE measurements provide insights into the distribution of collection losses throughout the CIS absorber layer. The results of this research can assist in the performance optimization of CIS devices as candidates for the bottom solar cell in tandem device configurations.

ACKNOWLEDGEMENT

This article is based on research supported by the National Science Foundation (NSF) under Award EECS-1665172.

REFERENCES

- [1] H. Hahn, G. Frank, W. Klingler, A.-D. Meyer, and G. Störger, "Untersuchungen über ternäre chalkogenide. V. Über einige ternäre chalkogenide mit chalkopyritstruktur," Zeitschrift für anorganische und allgemeine Chemie, vol. 271, no. 3-4, pp. 153-170, 1953.
- [2] B. Tell and H. Kasper, "Optical and electrical properties of AgGaS₂ and AgGaSe₂," *Physical Review B*, vol. 4, no. 12, p. 4455-4459, 1971.
- [3] B. Tell, J. Shay, and H. Kasper, "Room-temperature electrical properties of ten I-III-VI₂ semiconductors," *Journal of Applied Physics*, vol. 43, no. 5, pp. 2469-2470, 1972.
- [4] J. L. Shay and J. H. Wernick, Ternary Chalcopyrite Semiconductors: Growth, Electronic Properties, and Applications, Pergamon, New York, 1975.
- [5] S. Wagner, J. Shay, P. Migliorato, and H. Kasper, "CuInSe₂/CdS heterojunction photovoltaic detectors," *Applied Physics Letters*, vol. 25, no. 8, pp. 434-435, 1974.
- [6] J. Shay, S. Wagner, and H. Kasper, "Efficient CuInSe₂/CdS solar cells," *Applied Physics Letters*, vol. 27, no. 2, pp. 89-90, 1975.

- [7] L. Kazmerski, F. White, and G. Morgan, "Thin-film CuInSe₂/CdS heterojunction solar cells," *Applied Physics Letters*, vol. 29, no. 4, pp. 268-270, 1976.
- [8] R. Mickelson and W. Chen, "Development of a 9.4% efficient thinfilm CuInSe₂/CdS solar cell," *Proc. 15th IEEE Photovoltaic Specialists Conference*, pp. 800-804, 1981.
- [9] P. Jackson, R. Wuerz, D. Hariskos, E. Lotter, W. Witte, and M. Powalla, "Effects of heavy alkali elements in Cu(In, Ga)Se₂ solar cells with efficiencies up to 22.6%," *Physica Status Solidi (RRL) Rapid Research Letters*, vol. 10, no. 8, pp. 583-586, 2016.
- [10] Y. H. Jang, J. M. Lee, J. W. Seo, I. Kim, and D.-K. Lee, "Monolithic tandem solar cells comprising electrodeposited CuInSe₂ and perovskite solar cells with a nanoparticulate ZnO buffer layer," *Journal of Materials Chemistry A*, vol. 5, no. 36, pp. 19439-19446, 2017.
- [11] J. P. Mailoa, M. Lee, I. M. Peters, T. Buonassisi, A. Panchula, and D. N. Weiss, "Energy-yield prediction for II–VI-based thin-film tandem solar cells," *Energy & Environmental Science*, vol. 9, no. 8, pp. 2644-2653, 2016.
- [12] T. Todorov, T. Gershon, O. Gunawan, Y. S. Lee, C. Sturdevant, L.-Y. Chang, and S. Guha, "Monolithic perovskite-CIGS tandem solar cells via in situ band gap engineering," *Advanced Energy Materials*, vol. 5, no. 23, 1500799-1500804, 2015.
- [13] P. Aryal, A.-R. Ibdah, P. Pradhan, D. Attygalle, P. Koirala, N. J. Podraza, S. Marsillac, R. W. Collins, and J. Li, "Parameterized complex dielectric functions of CuIn_{1-x}Ga_xSe₂: applications in optical characterization of compositional non-uniformities and depth profiles in materials and solar cells," *Progress in Photovoltaics: Research Applications*, vol. 24, no. 9, 1200–1213 (2016).
- [14] P. Pradhan, P. Aryal, A.-R. Ibdah, P. Koirala, J. Li, N. J. Podraza, A. A. Rockett, S. Marsillac, and R. W. Collins, "Effect of molybdenum deposition temperature on the performance of CuIn_{1-x}Ga_xSe₂ solar cells," *Proc. 42nd IEEE Photovoltaic Specialists Conference*, Art. No. 5890, pp. 1-4, 2015.
- [15] A.-R. A. Ibdah, P. Koirala, P. Aryal, P. Pradhan, M. J. Heben, N. J. Podraza, S. Marsillac, and R. W. Collins, "Optical simulation of external quantum efficiency spectra of CuIn_{1-x}Ga_xSe₂ solar cells from spectroscopic ellipsometry inputs," *Journal of Energy Chemistry* (in press, available online: https://doi.org/10.1016/j.jechem.2017.10.029).